



Nanostructured antireflective in-plane solar harvester

JARED TIPPENS, ABHIJEET BAGAL, XU A. ZHANG, AND CHIH-HAO CHANG*

Department of Mechanical and Aerospace Engineering, North Carolina State University, Raleigh, North Carolina 27695, USA

**chichang@ncsu.edu*

Abstract: In this work, we demonstrate a two-dimensional nano-hole array that can reduce reflection losses while passively trapping and harvesting incident light. The surface structure is designed to scavenge a small portion of incident light that would typically be lost due to Fresnel reflection, while the majority of light transmits unobstructed like a regular window. The trapping mechanism is dependent on angle and wavelength, and can be designed to selectively trap narrow wavelength bands using the constructed theoretical models. We demonstrate that structures with periods of 275 nm and 325 nm can trap different wavelength range within the visible spectrum, while simultaneously suppressing reflection losses. The trapping effect can be observed visually, and can be converted to a current output using a photovoltaic (PV) cell on the glass edge. The fabrication of such materials employs a simple replication process, and can be readily scaled up for large-scale manufacturing. The demonstrated solar harvester can be potentially be widely deployed in residential and commercial buildings as multifunctional windows for solar energy harvesting, scavenging, spectra splitting, and anti-glare properties.

©2017 Optical Society of America

OCIS codes: (310.6628) Subwavelength structures, nanostructures; (220.3740) Lithography; (220.4241) Nanostructure fabrication; (350.6050) Solar energy.

References and links

1. H. Estiri, "The indirect role of households in shaping US residential energy demand patterns," *Energy Policy* **86**, 585–594 (2015).
2. L. Pérez-Lombard, J. Ortiz, and C. Pout, "A review on buildings energy consumption information," *Energy Build.* **40**(3), 394–398 (2008).
3. G. Smestad, H. Ries, R. Winston, and E. Yablonovitch, "The thermodynamic limits of light concentrators," *Sol. Energy Mater.* **21**(2), 99–111 (1990).
4. R. Buck, T. Bräuning, T. Denk, M. Pfänder, P. Schwarzbözl, and F. Tellez, "Solar-hybrid gas turbine-based power tower systems (REFOS)," *J. Sol. Energ-T. ASME* **124**(1), 2–9 (2002).
5. W. T. Xie, Y. J. Dai, R. Z. Wang, and K. Sumathy, "Concentrated solar energy applications using Fresnel lenses: A review," *Renew. Sustain. Energy Rev.* **15**(6), 2588–2606 (2011).
6. Y. Wu, S. Vorndran, S. Pelaez, J. Russo, and R. Kostuk, "Design of a holographic micro-scale spectrum-splitting photovoltaic system," *Proc. SPIE* **9175**, 9559 (2015).
7. N. Mohammad, P. Wang, D. J. Friedman, and R. Menon, "Enhancing photovoltaic output power by 3-band spectrum-splitting and concentration using a diffractive micro-optic," *Opt. Express* **22**(106), A1519–A1525 (2014).
8. P. S. Friedman, "Luminescent solar concentrators," *Opt. Eng.* **20**(6), 206887 (1981).
9. H. Li, K. Wu, J. Lim, H. Song, and V. I. Klimov, "Doctor-blade deposition of quantum dots onto standard window glass for low-loss large-area luminescent solar concentrators," *Nat. Energ.* **1**, 16157 (2016).
10. F. Meinardi, A. Colombo, K. Velizhanin, R. Simonutti, M. Lorenzon, L. Beverina, R. Viswanatha, V. I. Klimov, and S. Brovelli, "Large-area luminescent solar concentrators based on/Stokes-shift-engineered/nanocrystals in a mass-polymerized PMMA matrix," *Nat. Photonics* **8**(5), 392–399 (2014).
11. M. Debije and P. Verbunt, "Thirty Years of Luminescent Solar Concentrator Research: Solar Energy for the Built Environment," *Adv. Energy Mater.* **2**(1), 12–35 (2012).
12. L. Desmet, A. J. Ras, D. K. de Boer, and M. G. Debije, "Monocrystalline silicon photovoltaic luminescent solar concentrator with 4.2% power conversion efficiency," *Opt. Lett.* **37**(15), 3087–3089 (2012).
13. Y. Zhao, G. Meek, B. Levine, and R. Lunt, "Near-Infrared Harvesting Transparent Luminescent Solar Concentrators," *Adv. Opt. Mater.* **2**(7), 606–611 (2014).
14. Y. Zhao and R. Lunt, "Transparent luminescent solar concentrators for large-area solar windows enabled by massive stokes-shift nanocluster phosphors," *Adv. Energy Mater.* **3**(9), 1143–1148 (2013).

15. R. W. MacQueen, Y. Y. Cheng, R. G. Clady, and T. W. Schmidt, "Towards an aligned luminophore solar concentrator," *Opt. Express* **18**(S2 Suppl 2), A161–A166 (2010).
16. L. R. Bradshaw, K. E. Knowles, S. McDowall, and D. R. Gamelin, "Nanocrystals for luminescent solar concentrators," *Nano Lett.* **15**(2), 1315–1323 (2015).
17. M. J. Currie, J. K. Mapel, T. D. Heidel, S. Goffri, and M. A. Baldo, "High-efficiency organic solar concentrators for photovoltaics," *Science* **321**(5886), 226–228 (2008).
18. B. Cocilovo, A. Hashimura, D. J. Tweet, T. Voutsas, and R. A. Norwood, "Highly transparent light-harvesting window film," *Appl. Opt.* **54**(30), 8990–8998 (2015).
19. C. Yeh, F. Chang, H. Young, T. Hsieh, and C. Chang, "Transparent solar concentrator for flat panel display," *Jpn. J. Appl. Phys.* **51**(6), 06FL03 (2012).
20. T. Maruyama and S. Osako, "Wedge-shaped light concentrator using total internal reflection," *Sol. Energy Mater. Sol. Cells* **57**(1), 75–83 (1999).
21. R. Dewan and D. Knipp, "Light trapping in thin-film silicon solar cells with integrated diffraction grating," *J. Appl. Phys.* **106**(7), 074901 (2009).
22. X. Sheng, J. Liu, I. Kozinsky, A. M. Agarwal, J. Michel, and L. C. Kimerling, "Design and non-lithographic fabrication of light trapping structures for thin film silicon solar cells," *Adv. Mater.* **23**(7), 843–847 (2011).
23. L. Zeng, Y. Yi, C. Hong, J. Liu, N. Feng, X. Duan, L. Kimerling, and B. Alamariu, "Efficiency enhancement in Si solar cells by textured photonic crystal back reflector," *Appl. Phys. Lett.* **89**(11), 111111 (2006).
24. P. Vukusic and J. R. Sambles, "Photonic structures in biology," *Nature* **424**(6950), 852–855 (2003).
25. R. H. Siddique, G. Gomard, and H. Hölscher, "The role of random nanostructures for the omnidirectional anti-reflection properties of the glasswing butterfly," *Nat. Commun.* **6**, 6909 (2015).
26. A. Yoshida, M. Motoyama, A. Kosaku, and K. Miyamoto, "Antireflective nanoprotuberance array in the transparent wing of a hawkmoth, *Cephonodes hylas*," *Zool. Sci.* **14**(5), 737–741 (1997).
27. J. G. Kim, H. J. Choi, K. C. Park, R. E. Cohen, G. H. McKinley, and G. Barbastathis, "Multifunctional inverted nanocone arrays for non-wetting, self-cleaning transparent surface with high mechanical robustness," *Small* **10**(12), 2487–2494 (2014).
28. S. Jeong, S. Wang, and Y. Cui, "Nanoscale photon management in silicon solar cells," *J. Vac. Sci. Technol.* **30**(6), 060801 (2012).
29. K. C. Park, H. J. Choi, C. H. Chang, R. E. Cohen, G. H. McKinley, and G. Barbastathis, "Nanotextured silica surfaces with robust superhydrophobicity and omnidirectional broadband supertransmissivity," *ACS Nano* **6**(5), 3789–3799 (2012).
30. M. G. Moharam and T. K. Gaylord, "Rigorous coupled-wave analysis of planar-grating diffraction," *J. Opt. Soc. Am.* **71**(7), 811–818 (1981).
31. W. Lee and F. L. Degertekin, "Rigorous coupled-wave analysis of multilayered grating structures," *J. Lightwave Technol.* **22**(10), 2359–2363 (2004).
32. Q. Xie, M. H. Hong, H. L. Tan, G. X. Chen, L. P. Shi, and T. C. Chong, "Fabrication of nanostructures with laser interference lithography," *J. Alloys Compd.* **449**(1), 261–264 (2008).
33. J. de Boor, N. Geyer, U. Gösele, and V. Schmidt, "Three-beam interference lithography: upgrading a Lloyd's interferometer for single-exposure hexagonal patterning," *Opt. Lett.* **34**(12), 1783–1785 (2009).
34. A. Bagal and C. H. Chang, "Fabrication of subwavelength periodic nanostructures using liquid immersion Lloyd's mirror interference lithography," *Opt. Lett.* **38**(14), 2531–2534 (2013).
35. Y. Xia and G. M. Whitesides, "Soft lithography," *Annu. Rev. Mater. Sci.* **28**(1), 153–184 (1998).
36. T. W. Lee, O. Mitrofanov, and J. Hsu, "Pattern-Transfer Fidelity in Soft Lithography: The Role of Pattern Density and Aspect Ratio," *Adv. Funct. Mater.* **15**(10), 1683–1688 (2005).

1. Introduction

With growing energy demands and decreasing space available, the need for efficient energy harvesting with small footprint becomes increasingly important. Every year, 350 billion kilowatt-hours of electricity are used in the U.S for space cooling, and about 20% to 40% of total energy used is consumed by residential and commercial buildings [1,2]. With the rapid draining of fossil fuels and the advent of the associated environmental problems, clean and sustainable energy sources are demanding. Solar energy is one promising form of clean energy and has been an extremely active research area over the past decades. Despite the significant research progress in high-efficient solar cell materials, deployment over large area is expensive, difficult to implement, and in some cases unpractical. Solar concentrators and harvesters can meet this demand by redirecting light using geometrical and physical principles [3]. There are many different types of solar concentrators with immensely varying mechanisms of light trapping and guiding. The most traditional method involves reflecting sunlight using mirrors to a central tower. This tower receives the energy and uses the heat to generate electricity [4]. Fresnel lenses and other holographic elements can also be used to focus sunlight, with the additional benefit of spectra splitting into solar cells with matching

bandgap [5–7]. While existing solar concentrators are efficient in terms of concentration factors, they tend to be large and can be difficult to integrate seamlessly into existing surfaces.

To reduce panel footprint and facilitate integration, there has been a lot of interest in solar harvesters using planar elements for in-plane trapping. These types of harvesters can make use of unused window surface area that covers large portions of commercial and residential buildings. This has been demonstrated previously using luminescence solar concentrators (LSC), which upon ultraviolet (UV) excitation emits visible light that can be trapped in the in-plane direction [8–17]. While concentration effects are possible, these planar approaches tend to have lower concentration factors. Another approach is based on surface structures such as surface microstructures, textured films, and glass prisms to refract and trap light [18–20]. These mechanisms aim to redirect and channel light within the glass substrate to a photovoltaic (PV) cell on the edge using total internal reflection (TIR). Diffractive structures have also been explored, where periodic structures residing directly on silicon solar cells have demonstrated increased energy conversion by increasing in-plane light path [21–23]. While existing in-plane solar harvesters are effective, optical losses due to the scattering and trapping mechanisms can diminish the overall transmission. In addition, these approaches can also obstruct or change the visual appearance of the window.

Antireflection (AR) nanostructures with subwavelength period are another exciting research area relevant to transparent surfaces. Such structures can reduce the Fresnel reflection losses between media with different refractive indices by serving as a gradient-index medium, thereby increasing transmission. This phenomenon has been observed in nature in moth eyes, glass-wing butterfly wings, and hawkmoth wings [24–26]. Inspired by such principles, periodic cones and holes engineered in the laboratory have also been shown to act as AR surfaces to minimize optical reflection losses over a broad range of wavelengths and incident angles [27–29]. This is useful in enhancing transmission and reducing glare in comparison with ordinary glass planar surfaces.

In this work, we demonstrate an integrated light guiding structure for an in-plane solar harvester while simultaneously acting as an anti-reflection surface, as illustrated in Fig. 1. This harvester is based on periodic two-dimensional (2D) nano-hole array in a polymer material that can be applied on glass substrates. The structure period is designed to be close to the operating wavelength so that the reflection and transmission orders behave differently. For the reflection orders in air, the structure is subwavelength so no diffraction occurs, acting like an AR structure to suppress reflection losses. For the transmitted orders in the higher index medium, the structures act as a diffraction grating for oblique incident light, where the transmitted 1st-order diffraction order is directed towards the glass edge, as illustrated in Fig. 1(b). Through TIR, the diffracted order can then be channeled within the glass and converted into electrical energy using a PV cell. The goal of this design is to harvest or scavenge a small fraction of the incident light that would typically be lost through Fresnel reflection, while the majority goes through unobstructed. A theoretical model based on rigorous coupled-wave analysis (RCWA) has been constructed to design the structure height and period and optimize trapping efficiency for various wavelength bands and incident angles. Structures with two different periods have been fabricated, and their optical and electrical properties characterized to demonstrate successful in-plane trapping. The proposed AR in-plane solar harvester can find applications in passive energy scavenger through glass windows of residential and commercial buildings.

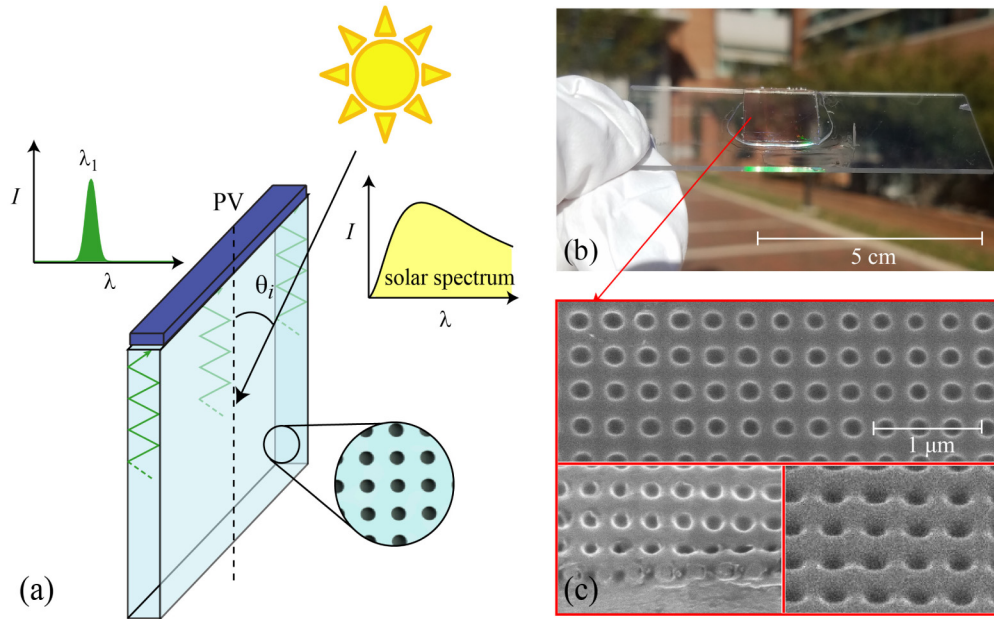


Fig. 1. Schematic of (a) the proposed antireflection in-plane solar harvester, where incident sunlight is trapped to a glass edge through TIR and received by a PV cell. (b) Photograph of fabricated solar harvester without PV cell attached. Under ambient illumination from the sun, trapping of green light can be observed on the bottom glass edge. (c) Scanning electron micrographs of the nano-hole array with 325 nm period.

2. Optical design and simulation

A simulation model was constructed to examine AR, diffraction, and TIR effects to predict the light trapping performance for different structure geometries. The simulation is based on RCWA [30,31], where reflection and transmission efficiencies at a 2D diffraction grating bounded by two different media is examined. In the proposed structure, trapping starts abruptly once light reaches the incidence angle where the transmitted 1st-order diffraction occurs, and is limited at high incident angle when the diffracted orders can no longer be trapped inside glass. The diffraction angle of the m -th order is governed by the grating equation:

$$\theta_m = \sin^{-1} \left(\frac{m\lambda}{\Lambda n_2} + \frac{n_1 \sin \theta_i}{n_2} \right) \quad (1)$$

Where n_1 and n_2 are the media indices, λ is the wavelength, and Λ is the structure period. There are three key interactions of interest in determining the trapping efficiency of the structure, as depicted in Fig. 2. The first is the transmitted 1st-order diffraction T passing through the air/structure surface, which will propagate towards the back surface at an oblique angle if the wavelength is close to the structure period. The simulated transmitted total and 1st-order diffraction efficiencies for TE-polarized light, 550 nm wavelength, and 325 nm period structure are plotted vs incident angle in Fig. 3(a). It can be observed that at normal incidence the 1st-order does not exist, allowing the structure to function as a zero-order subwavelength structure. At around 10° the 1st-order is no longer evanescent and becomes a propagating wave traveling at oblique angles towards the back surface. Note the diffraction efficiency is designed to be small, with a peak in the order of 10%, so that most light is transmitted and the structure functions as an energy scavenger.

The second interaction is when the transmitted 1st-order diffraction reach the bottom glass/air surface, as depicted in Fig. 2, and whether TIR occurs to trap the light within the glass substrate. This is generally the case when the diffracted order just becomes propagating and have high incident angle within the glass. Given that TIR occurs at the bottom surface, the light is then reflected towards the top structure/air surface. This is the third interaction of interest, as depicted in Fig. 2, and the efficiency of the reflected 0th-order R determines if light can be trapped. Note that since the interface is a surface nanostructure, light leakage and other internally reflected diffraction orders can exist and must be minimized. The simulated total and 0th-order internal reflection efficiencies are plotted as a function of the incident angle of the original beam in air in Fig. 3(b). It can be observed that at incident angles immediately after the 1st-order diffraction becomes propagating at around 10 degrees, the internal incident angle in glass is high enough to efficiently reflect 80-90% of the light. Note that while the internal incident angles are the same, the trapping at the structure surface results in other reflected and transmitted diffraction orders, and is not as 100% efficient as TIR at the bottom surface. As incidence angle is increased past the initial peak, the reflection efficiency drops dramatically, resulting in a loss of overall trapping efficiency at higher angles.

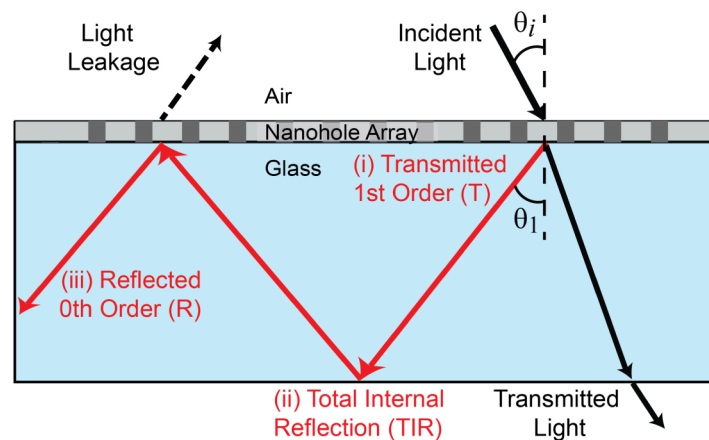


Fig. 2. Schematic of light path illustrating the three key interactions: (i) transmitted 1st-order diffraction from the top nanostructure surface, T , (ii) TIR from the bottom glass/air interface, and (iii) internally reflected 0th-order diffraction at the top surface.

In addition to the transmitted 1st-order diffraction and reflected 0th-order efficiencies, the number of reflection the light experience is also of critical importance. Each bounce will reduce the amount of trapped light, as the reflection efficiency R at the top nanostructure surface is not 100%, as shown in Fig. 3(b). This is especially problematic as the propagation angle in glass decreases and results in more reflections of the trapped light. The number of reflections that light will undergo can be approximated by $N = L/(2t \tan \theta_1)$, where θ_1 is the internal angle, t is the glass thickness, and L is the travel distance. It was found that for a 15 mm glass sample with 1 mm thickness, the light can experience from 1 to 10 reflection, depending on the incident angle and structure period. Combining these effects the overall trapping efficiency η of the sample, an import figure of merit to determine system performance for the proposed system, is given by,

$$\eta = T \cdot R^N \quad (2)$$

where transmission T and reflection R are the simulated transmitted and reflected efficiencies at the nanostructured surface, respectively. The total optical efficiency for 550 nm TE-polarized light and 325 nm period structure is depicted in Fig. 3(c). It can be observed that for this wavelength the trapping range is limited to incident angles of ~ 10 - 45° , with a peak

efficiency around 4.7%. Note while this number appears low, it satisfies the proposed goal of utilizing the structure as a passive solar energy harvester without obstructing light transmission. It should also be noted that the transmission will drop slightly while the incidence angle is in the range where trapping occurs.

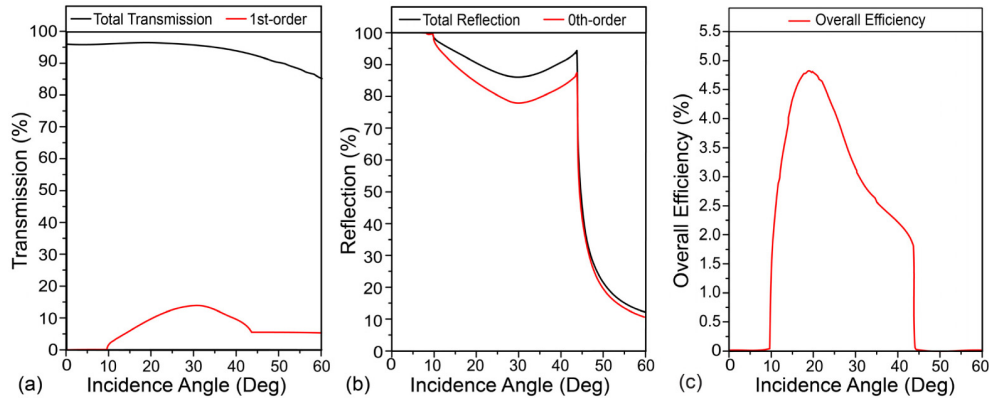


Fig. 3. Simulated efficiencies for 550 nm wavelength, TE-polarized light on 325 nm period structure. (a) Total and 1st-order diffraction efficiency at the top structure surface, (b) total and 0th-order internal reflection efficiency, and (c) overall optical efficiency vs incident angle on the structure in air.

By evaluating the efficiency at these three interactions, the overall trapping efficiency can be calculated for any given wavelength and incident angle. The simulation was set up in Matlab, where parameters of wavelength, incident angle, structure period, height, profile can be modified. Structure periods and depth from 200 to 400 nm and 50 to 500 nm were simulated, respectively, for device operation in the visible spectrum. Both transverse electric (TE) and transverse magnetic (TM) polarized light were examined. It is important to note that different structure heights could be used in different applications. In general it was found that transmission diffraction efficiency T increases with higher structure height, while the internal reflection efficiency R decreases. Therefore a height in the range of 200 nm was selected where both transmission and reflection values were cumulatively optimized for the size of the glass slide. Additionally, holes and pillar geometries were compared and have comparable overall efficiencies, while the hole geometry having the added benefit of greater structural strength [27]. The final structure designs are 2-D hole array with depth of 200 nm and periods of 275 nm and 325 nm, which were found to trap more effectively within the visible spectrum.

3. Experimental methods

The nano-hole arrays were fabricated using a two-step replication procedure on glass substrate. In the first step, a 2D nano-pillar array was patterned in positive-tone photoresist (Sumitomo PFI88) on a silicon wafer using Lloyd's mirror interference lithography [32–34]. A thin layer of antireflection coating (ARC, Brewer i-con 16) was used to reduce standing wave from back reflection. In the second step, a process similar to soft lithography is used to transfer the nano-pillar mold into an optically clear UV-cured epoxy (NOA71, Norland Products, Inc.) [35,36]. This is done by placing the uncured, highly viscous NOA between a microscope glass slide and the photoresist pillar substrates. The surface of the 2D nano-pillar mold has been treated with silane to mitigate adhesion. The NOA records the inverse profile, and is then cured using ultraviolet (UV) light. The silicon substrate is then peeled off, leaving a cured NOA film with 2D nano-hole array on glass. The NOA bonds well to glass, has high optical clarity, and has refractive index value ($n = 1.56$) close to that of standard microscope slide ($n = 1.525$) used as substrate. Figure 1(b) illustrate the trapping effect of the sample

when placed in ambient sun light. The fabricated surface area is roughly 4 cm^2 , and a picture of the sample trapping green light at the edge under ambient sunlight is shown in Fig. 1(b). The nanostructure is shown in Fig. 1(c) for a 325 nm sample, with images taken by a scanning electron microscope (FEI Verios 460L). To convert the trapped light to electrical energy, an ultra-thin off-the-shelf silicon PV cell can be bonded to the long edge of the glass slide using NOA.

4. Experimental results

The AR properties of the fabricated samples with 325 nm period were examined. First, the broadband transmittance was characterized using a spectrophotometer (Agilent Cary 5000) at normal incidence, as shown in Fig. 4(a). The incident wavelength was varied from 200 to 800 nm, spanning the full spectrum from UV to near-infrared (NIR) range. The transmittance for a microscope glass slide was also recorded for comparison. At normal incidence, longer wavelengths are shown to have enhanced transmission compared to glass by around 1.5%. This demonstrates the AR effects of the nanostructures when the wavelength is longer than the structure period. However, as the incident wavelength decreases below 500 nm, the transmitted 1st-order diffraction is no longer evanescent in the NOA layer. At this point the light trapping starts to occur, decreasing the transmission for shorter wavelengths. The transmission is further reduced at wavelength lower than 400 nm, when the transmission of NOA is greatly reduced.

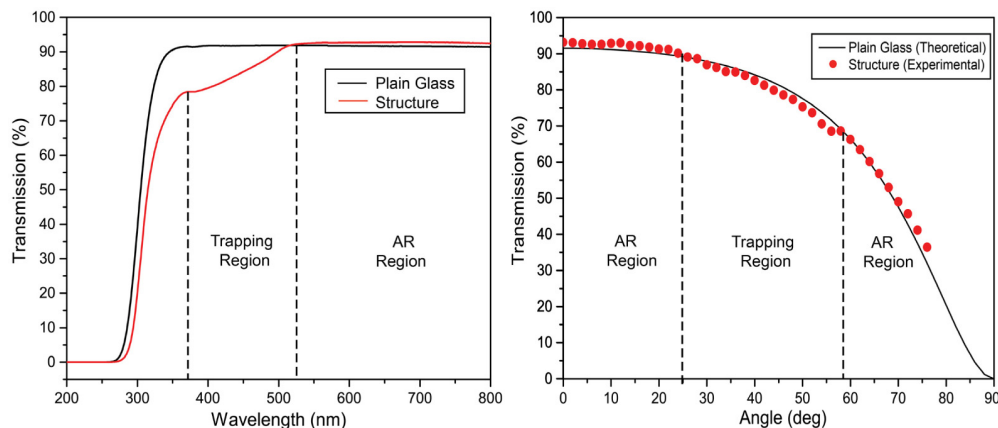


Fig. 4. Measured broadband and wide-angle transmission for 325 nm period. (a) Transmittance through the 325nm structure is compared with bare glass over a sweep of wavelengths from 200 to 800 nm using UV-vis-NIR photospectrometer. (b) Transmission efficiency as functions of incident angle at 633 nm in comparison to plain glass given by Fresnel's equations.

The transmission of the same sample versus incident angle was also characterized vs incident angle. The laser source (633 nm HeNe laser with TE polarization) and detector remained stationary while the sample was rotated on a stage from 0 to 76° , the maximum possible for the sample area. The transmission was recorded and compared to the theoretical transmission of glass given by Fresnel's equations. Figure 4(b) shows the results of the transmission measurements as a function of incident angle. The transmission can be seen to be greater than that of glass for incident angles close to normal and also at oblique angles. The 1.5-2% in transmission enhancement demonstrates AR effects, and the improvement is similar to the broadband measurements. However, the transmission through the structure is slightly lower than that of plain glass from 30° to 60° , which coincides with the angle range where trapping occurs. This implies that the light reflection that is typically lost due to Fresnel mismatch is partially being redirected and trapped in-plane for harvesting. While the structures demonstrate effective AR properties, light trapping does reduce overall

transmission when light is being directed to the PV cell. AR effect could be further improved by using structures with higher aspect ratio and smoother taper.

The optical trapping of the fabricated structures can be visually observed. Figure 5 shows the simulated trapping efficiencies at various incident angle, with the corresponding observed image of the visible light trapped when the sample is illuminated with white light. At different incident angles, different wavelengths are trapped more efficiently, and the color of the trapped light at the edge varies. This is supported by the RCWA model for the 325 nm period structure, where the peak wavelengths of 450, 500, 550, 600, and 650 nm occur at incident angles of 0°, 10.1°, 19.5°, 28.6°, and 38.9° respectively. These peaks at various wavelengths qualitatively align well with the experimental observation, and the inset images are taken at angles of 0°, 10°, 20°, 30°, and 40°. For incidence angles above 40 degrees, only red light appears on the glass edge, which is also confirmed by the model. The movie of the visual light trapping effect can be seen in [Visualization 1](#). These results illustrate the wavelength selective characteristics for different incident angles, which can be utilized for spectra splitting of a broadband source.

The absolute optical efficiency measured were around $\eta = 1.9\%$ at 633 nm wavelength, lower than predicted value. This can be attributed to difficulty in complete capture of trapped light at the edge. As governed by Eq. (1), the trapped light leaves the glass edge at two equal and opposite angles, creating two spots (see [Visualization 2](#)). To characterize the overall efficiency, the detector measures the intensity of both spots at the peak angle, and these values are then added together. Both spots were measured 3-5 cm from the glass edge, as the detector could not be brought directly to the glass edge without obstructing with the incident beam. This results in an unmeasured portion of the light being lost before hitting the detector. There are also other sources of error, such as film thickness effects and light leakage at the film edges, which were not taken into account in the model.

A key figure of merit, analogous to those used in LSC, is the concentration factor $C = \eta G$. This is a valuable indicator of whether the surface nanostructures is enhancing light intensity at the PV cell. The geometric gain of the system G can be estimated by dividing the out-of-plane collection area by the glass edge area, and is calculated to be 16.7 for the fabricated samples. In the current prototype, the concentration factor C is around 0.32, indicating the intensity of the trapped light is not being enhanced. While this is less than state-of-the-art LSC, it can be improved further by optimizing G , which is kept constant in this work. By increasing structure area and decreasing the glass thickness, a concentration factor greater than unity can potentially be achieved, and is the subject of future research. Beyond system performance, the proposed method has a number of advantages over LSC. Being a surface structure, it can be applied over existing windows as a thin film without changing the bulk composition of the glass. In addition, wavelength selectivity can be achieved by changing the nanostructure geometry, which for LSC requires alteration of chemical composition of luminescent material.

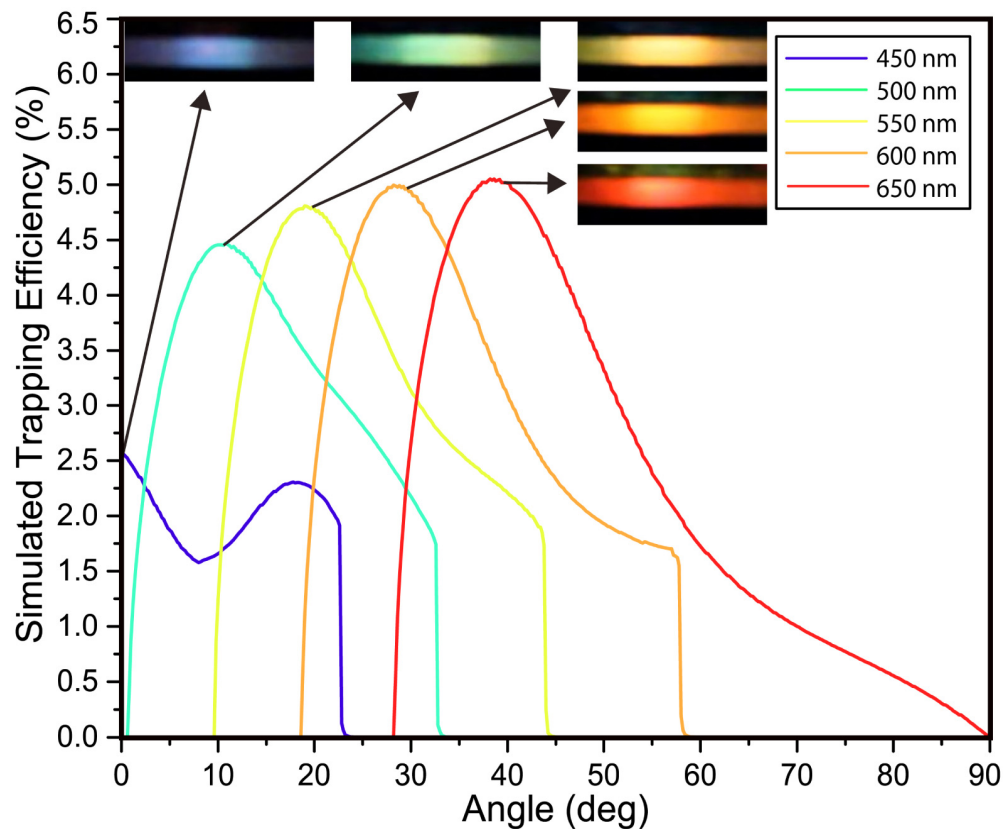


Fig. 5. Simulated efficiencies vs incident angles and corresponding visual observation of trapped light at the edge when white light is illuminated over the sample. The trapped blue, green, yellow, orange, and red at the edge were observed at viewing angles of 0° , 10° , 20° , 30° , and 40° , respectively (see Visualization 1). The RCWA simulation analyzed 325 nm period structure under various wavelengths ranging from 450 to 650 nm.

The fabricated structure was packaged with a PV cell to test the energy harvesting capability. The silicon PV cell used is an off-the-shelf component, and measures 1 mm wide, 55 mm long, and 50 μm thick. The solar cell is bonded to the long edge of the glass slide using NOA, and copper wires are connected to each terminal using a heat-curable silver epoxy (MG Chemicals 8331-14G). The current output for the device with 275 nm-period structure is measured for TE-polarized 532 nm laser (20 mW) with incidence angles from 0° to 60° . The device with 325 nm-period structure is tested using 532 nm and 633 nm (17 mW) lasers from 0° to 45° , also TE polarized. The surface area of the structure and proximity to the PV cell affects the possible range of testing angles achievable.

The angle-dependent trapping of the fabricated device has been examined by measuring the current output, as shown in Fig. 6. The electrical measurements are plotted with the simulated optical trapping efficiency to qualitatively compare the angle-dependent response. Figure 6(a) shows the 275 nm sample results for the 532 nm wavelength laser, Fig. 6(b) shows the 325 nm sample results for the 532 nm wavelength laser, and Fig. 6(c) shows the 325 nm results for the 633 nm wavelength laser. All three data show that the first wavelength peak denoting the onset of trapping matches well with the RCWA simulation. Additionally, the current output of the 275 nm sample can be seen to match the shape of the simulation by having a peak from 29° to 43° , and then falling to no current output from 45° until 60° . The 275 nm sample yields a maximum current output of 36 μA for the 532 nm laser. The electrical measurement for the 325 nm sample can be observed to have intensity oscillations for both

the 532 nm and the 633 nm wavelength laser, which does not correspond with the simulation result. This can be attributed to thin-film interference effects of the non-uniform-NOA layer, which can be observed visually at a certain viewing. The current output peaks at 93 μA for the 325 nm sample with the 532 nm laser, and can be seen to drop off at around 40° , which matches well with the simulation. The peak current for the samples was found to be 100 μA for the 633 nm laser. In Fig. 6 (c), the simulated trapping occurs from 25° to 70° , which corresponds to the slightly reduced transmission in the broadband transmission shown Fig. 4(b). Note while the electrical currents measured are relatively low, the angular profile matches well to the theoretical optical prediction to demonstrate angle and wavelength-selective trapping. The electrical performance can be further enhanced by using higher quality PV cells designed specifically for edge collection and optimizing the geometric gain G , and is the subject of future work.

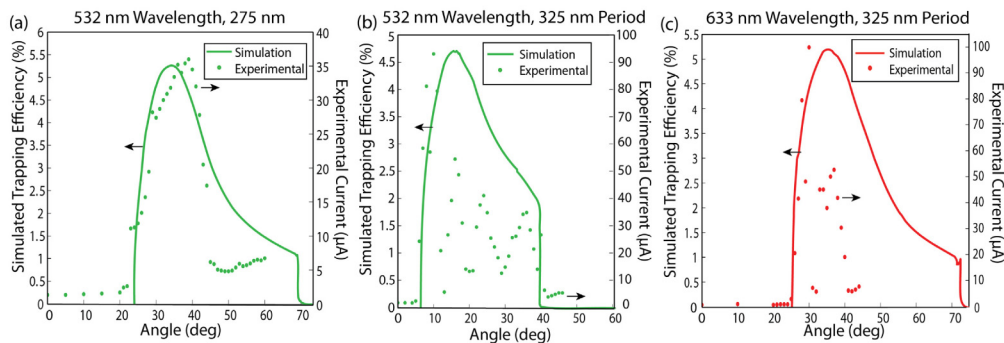


Fig. 6. Experimental electrical measurements and qualitative comparison with simulated optical trapping efficiency for packaged samples. The experimental data is overlaid with calculated curves using RCWA simulations: (a) Trapping of 532 nm light through a 275 nm period structure. (b) Trapping of 532 nm light through a 325 nm period structure. (c) Trapping of 633 nm light through a 325 nm period structure. The beam shapes of the trapped beam can be seen in [Visualization 2](#).

The in-plane solar harvester can also be designed to trap different color at the same incident angle by using different structure period. Figure 7 illustrates the trapping comparison between the 275 and the 325 nm-period samples under white light illumination at incident angle of 15° . It can be observed that the 275 nm sample traps blue light, while the 325 nm sample traps green light. This demonstrates spectra splitting, where the most efficiently trapped wavelength at each incident angle is dependent on the structure period and can be accurately designed. This can find application in double-pane windows, where two different structure geometries could effectively trap different wavelengths at the same incidence angle. This light could then be converted to electrical output using matching energy band gap solar cells at the edges. The structure parameters of the in-plane solar harvester can also further designed to include changing incident angles due to the sun's motion to optimize total energy converted, which is the subject of future work.

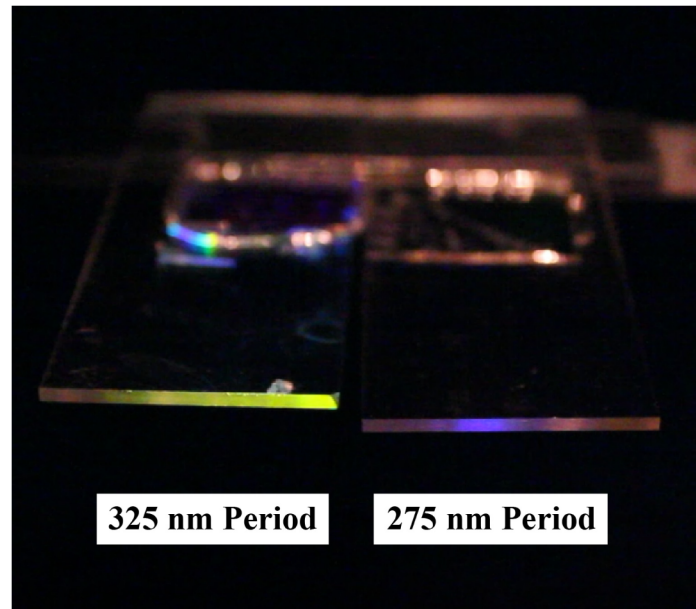


Fig. 7. Visual trapping comparison of 325 and 275 nm period samples under white light at $\sim 15^\circ$ incident angle. At this particular incident angle, the 325 nm period sample most effectively traps green light, while the 275 nm period sample most effectively traps blue light.

5. Conclusion

We have demonstrated an in-plane solar harvester using 2D nano-hole array to simultaneously trap incident light and reduce surface reflection. Unlike conventional solar concentrators which emphasize to redirect most solar energy with high concentration factor, the proposed approach balances the function of window as a viewing element with the added functionality of solar energy harvesting. The goal is so that a small amount of energy generated from the window can power small electronic devices while the viewing clarity is not obstructed. The structure also has AR properties, and can enhance transmission over broad wavelength and angle range. We have shown the solar harvester can output current from different wavelengths within the visible spectrum, as well as trap different wavelengths more efficiently at different incidence angles. The demonstrated device requires simple, low-cost replication process, and its manufacturing can be potentially scaled up by roll-to-roll nanoimprint integrated with glass window production lines. The proposed device has small footprint, and can be widely integrated into existing windows in buildings and other civil structures.

Funding

National Science Foundation (NSF) (1552424).

Acknowledgements

This work was performed in part at the NCSU Nanofabrication Facility (NNF) and the Analytical Instrumentation Facility (AIF), members of the North Carolina Research Triangle Nanotechnology Network (RTNN), which is supported by the National Science Foundation (Grant ECCS-1542015) as part of the National Nanotechnology Coordinated Infrastructure (NNCI). This work was supported by a NSF Faculty Early Career Development (CAREER) Program (grant CMMI#1552424).